

The atmospheric correction of water colour and the quantitative retrieval of suspended particulate matter in Case II waters: Application to MERIS

G. F. Moore , J. Aiken & S. J. Lavender

To cite this article: G. F. Moore , J. Aiken & S. J. Lavender (1999) The atmospheric correction of water colour and the quantitative retrieval of suspended particulate matter in Case II waters: Application to MERIS, International Journal of Remote Sensing, 20:9, 1713-1733, DOI: [10.1080/014311699212434](https://doi.org/10.1080/014311699212434)

To link to this article: <https://doi.org/10.1080/014311699212434>



Published online: 25 Nov 2010.



Submit your article to this journal 



Article views: 415



View related articles 



Citing articles: 27 View citing articles 

The atmospheric correction of water colour and the quantitative retrieval of suspended particulate matter in Case II waters: application to MERIS

G. F. MOORE†§, J. AIKEN† and S. J. LAVENDER‡

†Plymouth Marine Laboratory, Prospect Place, Plymouth, Devon PL1 3DH, England, UK

‡NERC Remote Sensing Data Analysis Service, Plymouth Marine Laboratory, Plymouth, Devon, England, UK

(Received 14 August 1996; in final form 25 August 1998)

Abstract. The remote sensing of turbid waters (Case II) using the Medium Resolution Imaging Spectrometer (MERIS) requires new approaches for atmospheric correction of the data. Unlike the open ocean (Case I waters) there are no wavelengths where the water-leaving radiance is zero. A coupled hydrological atmospheric model is described here. The model solves the water-leaving radiance and atmospheric path radiance in the near-infrared (NIR) over Case II turbid waters. The theoretical basis of this model is described, together with its place in the proposed MERIS processing architecture. Flagging procedures are presented that allow seamless correction of both Case I waters, using conventional models, and Case II waters using the proposed model. Preliminary validation of the model over turbid waters in the Humber estuary, UK is presented using Compact Airborne Spectrographic Imager (CASI) imagery to simulate the MERIS satellite sensor. The results presented show that the atmospheric correction scheme has superior performance over the standard single scattering approach, which assumes that water-leaving radiance in the NIR is zero. Despite problems of validating data in such highly dynamic tidal waters, the results show that retrievals of sediments within $\pm 50\%$ are possible from algorithms derived from the theoretical models.

Nomenclature

$\Delta\phi$	Azimuth difference
$\varepsilon(\lambda_1, \lambda_2)$	Ratio of $\rho_{rc}(\lambda_1)$ to $\rho_{rc}(\lambda_2)$ (equivalent to $\varepsilon_{as}(\lambda_1, \lambda_2)$ in Case I waters)
$\varepsilon_{as}(\lambda_1, \lambda_2)$	Ratio of $\rho_{as}(\lambda_1)$ to $\rho_{as}(\lambda_2)$
$\varepsilon_w(\lambda_1, \lambda_2)$	Ratio of $\rho_w(\lambda_1)$ to $\rho_w(\lambda_2)$
θ_s	Sun angle
θ_v	View angle
$\tilde{\rho}$	Fresnel reflectance for the sun and sky reflectance
ρ	Fresnel reflectance at normal incidence

§E-mail: G.Moore@ccms.ac.uk

ρ_a	Aerosol path reflectance
ρ_{as}	Single scattering aerosol reflectance ($\rho_{ra} + \rho_a$)
ρ_g	Reflectance due to Sun glitter
ρ_r	Rayleigh path reflectance
ρ_{ra}	Path reflectance from Rayleigh aerosol interaction
ρ_{rc}	Rayleigh corrected reflectance ($\rho_t - \rho_{tr}$)
ρ_t	Total top-of-atmosphere reflectance
ρ_w	Reflectance above water surface
τ_{oz}	Ozone optical thickness
τ_r	Rayleigh optical thickness
a_{chl}	Chlorophyll specific absorption
a_g	Coloured organic material (CDOM) specific absorption
a_s	Sediment specific absorption
a_w	Water specific absorption
b_b	Backscatter
\tilde{b}_b	Backscatter ratio
b_{bs}	Sediment specific backscatter
b_{bw}	Water backscatter
b_s	Sediment specific scattering
b_w	Water specific scattering
c	Empirical constant (Gordon and Wang 1994)
chl	Chlorophyll biomass concentration
Ed	Downwelling irradiance
$f(\mu_0, \lambda)$	Factor determined by the incident light field
g	Constant which consists of the ratios of air-sea interface effects
G	CDOM concentration
Lu	Upwelling radiance
L_{wn}	Normalized water-leaving radiance
n_w	Refractive index of seawater
Q	Ratio of upwelling irradiance to radiance
r	Air-water reflectance for diffuse irradiance
$R(\lambda)$	Irradiance reflectance
$R_{rs}(\lambda)$	Remote sensing reflectance
SPM	Suspended particulate matter (concentration)
t	Diffuse atmospheric transmittance

1. Background

The successful exploitation of remotely sensed observations of water colour requires the development of atmospheric correction methods in coastal waters, and the determination of suspended particulate matter (SPM) concentrations in gravimetric units for use in mass flux studies and hydrodynamic models. By definition, Case I waters (stratified shelf seas and the deep ocean) are coloured by biogenic materials alone (phytoplankton, its pigments, dissolved organic exudates and detritus). Coastal waters are usually termed Case II because the major influence on the water colour is SPM (tidally stirred sediments or riverine fluvial muds) or gelbstoff (yellow substances). These are mainly coloured dissolved organic material (CDOM), consisting of humic and fulvic compounds of terrestrial origin, that are transported into marine waters by river/estuary systems. With even modest concentrations of SPM ($> 2 \text{ g m}^{-3}$), the significant backscatter results in reflectance at

near-infrared wavelengths (NIR) negates the 'dark pixel' atmospheric correction procedures, which assume zero water-leaving radiance at NIR wavelengths (> 700 nm). These waters that reflect at NIR wavelengths are termed 'bright pixel' waters and require special atmospheric correction procedures. When phytoplankton such as coccolithophores are abundant, at any site, the water is highly reflective due to backscatter from the detached coccoliths at visible and NIR wavelengths and the 'bright pixel' atmospheric correction procedure is invoked. Very high concentrations of any phytoplankton particles will also give significant backscatter and again the 'bright pixel' atmospheric procedure will be required to correct for the resultant NIR reflectance. The influence of gelbstoff has little effect on the atmospheric correction ('dark pixel'), but special algorithms are needed for the retrieval of the concentrations of gelbstoff and other optically active components of the water.

2. Overall MERIS structure

Figure 1 shows the overall structure of the algorithms. The algorithms for processing Case II pixels represent only part of the full processing chain. In order to test the Case II Medium Resolution Imaging Spectrometer (MERIS) algorithms, data from the Compact Airborne Spectral Imager (CASI) have been used. Here, for test purposes the Case I aerosol atmospheric correction described by Antoine and Morel (1998) has been replaced by the Costal Zone Colour Scanner (CZCS) type single scattering approach described by Gordon and Wang (1994). The neural network described by Schiller and Doerfer (this issue) has been replaced by a simple ratio algorithm.

3. Hydrological model

The development of in-water models for the NIR requires parameters from field and laboratory measurements. Data for the absorption (Palmer and Williams 1974) and backscatter of pure water (Morel 1974) are available from the literature. Gordon and Ding (1992) indicate that instrument self shading is a serious problem for in-water radiance and irradiance measurements in the NIR, where the absorption of pure water is high, so field data are subject to larger errors of uncertainty. The approach in this study has been to use laboratory measurements of surface remotely sensed reflectance (R_{rs} , the ratio of upwelled radiance to downwelled irradiance) using a range of sediment types from a number of UK coastal sites that represent diverse sediment mineralogies (Bale *et al.* 1994). Measurements of reflectance with a spectroradiometer under laboratory conditions using a tank of depth 2 m are acceptable, due to the low penetration of light in pure water at NIR wavelengths; the optical depth is 1.53 m at 700 nm and falls to 0.23 m at 865 nm.

The tank experiments show that the relationship between absolute reflectance of particle suspensions and their gravimetric concentrations varies between different sediment types and between size fractionated sediments of the same type. However, the reflectance of the small fractions, which are the normal component in natural suspensions, are quite consistent. Figure 2(a) shows the reflectance spectra from three groups, representing the course, medium and fine suspended sediment fractions. The smaller size fraction of each sediment has a greater reflectance for the same SPM concentration. For most marine waters only fine sediments are in suspension in the surface layer.

Figure 2(b) shows the ratio of remotely sensed reflectance between MERIS bands 13 and 14 (775 and 865 nm (Rast and Bezy 1999)). The figure shows a consistent

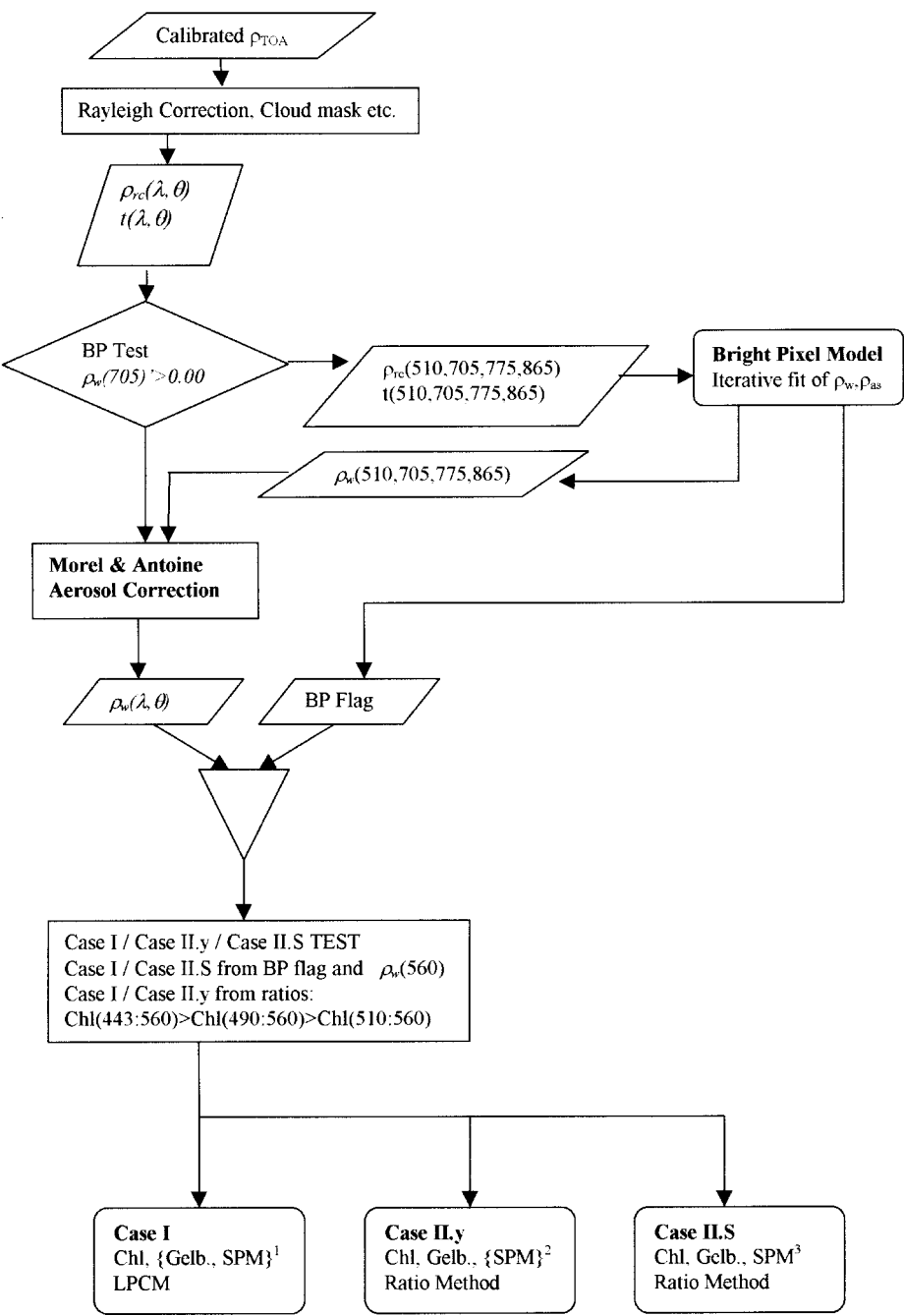


Figure 1. Bright pixel processing and in-water Case II processing chain. Key to figure: ¹By definition gelbstoff and SPM are low, but biogenic DOC and phytoplankton may be retrieved. ²By default SPM is low since the Case II.S test (see §5.1) pre-selects data for this. ³SPM would equate to coccolith concentration in oceanic and shelf seawaters, and SPM could be equated to alternative units, i.e. coccolith number m^{-3} .

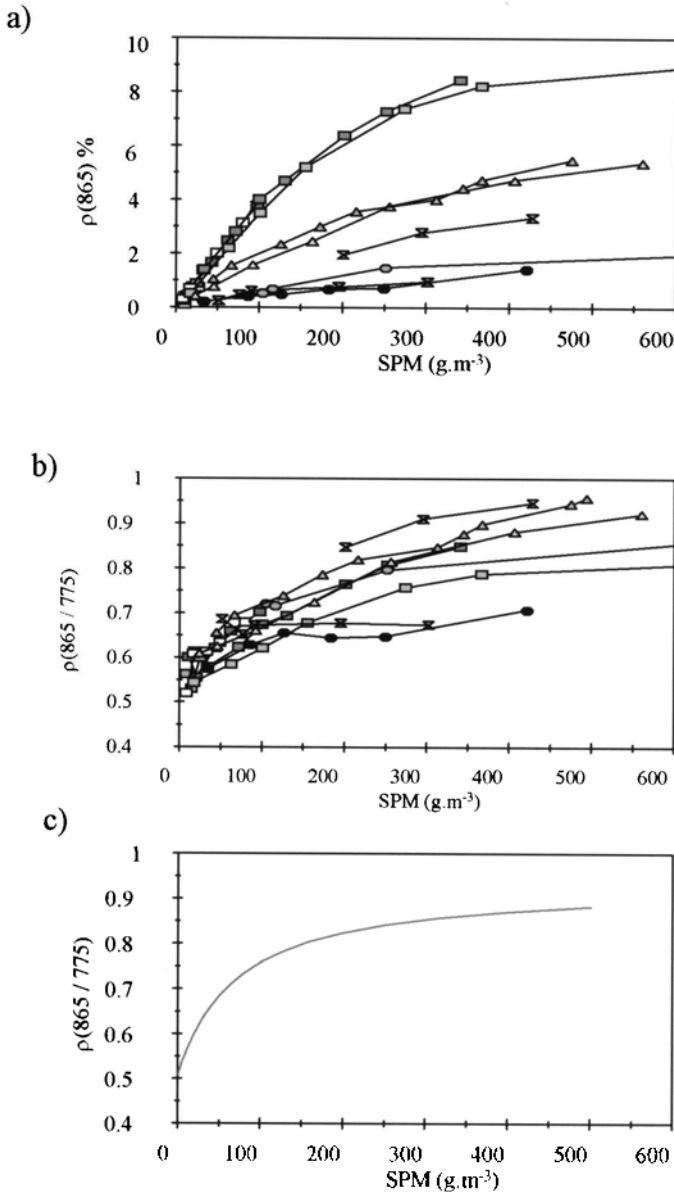


Figure 2. (a) $\rho(865)$ plotted against SPM for the tank data set, with each curve representing a different sediment type (squares are fine fractions; triangles are medium fractions; circles are coarse fractions; hourglasses are unfractionated sediment). (b) Band ratio (865/775) plotted against SPM for the tank data set with each curve representing a different sediment type (as in figure 2(a)). (c) Band ratio (865/775) plotted against SPM curve derived from the model.

relationship with gravimetric load for a number of sediment types with modal particle diameters varying from 5 to $100 \mu\text{m}$. The sediment data that fall markedly below the main group are from artificial coarse sediment. This would be encountered rarely in the natural situation, but one example would be re-suspension over shallow banks.

The relationship between gravimetric SPM and reflectance ratios is a direct consequence of the relationship between the inherent optical properties (IOPs) of the particles at the wavelengths of the two bands. This can be demonstrated analytically.

The reflectance at a particular wavelength can be expressed as:

$$\rho_w = \left(\frac{(1 - \rho)(1 - \tilde{\rho})R}{n_w^2(1 - rR)Q} \right) \quad (1)$$

where n_w is the refractive index of seawater, R is the irradiance reflectance, ρ is the Fresnel reflectance at normal incidence, $\tilde{\rho}$ is the Fresnel reflectance for sun and sky irradiance, r is the air–water reflectance for diffuse irradiance and Q is the ratio of upwelling irradiance to radiance. Q varies with the angular distribution of the upwelling light field. It is equal to π for an isotropic distribution, but may be up to five for bright pixel waters (Morel and Gentili 1993). The term $(1 - rR)$ is normally assumed to be unity for Case I waters, but has to be included for bright pixel waters because of their high irradiance reflectance (up to 10%). The irradiance reflectance in the NIR can be expressed as the following, using the formulation of Morel and Gentili (1993):

$$R = f(\mu_0, \lambda) \left(\frac{0.5b_w + \tilde{b}_s b_s \text{SPM}}{a_w + a_s \text{SPM}} \right) \quad (2)$$

where f is a factor determined by the incident light field (μ_0) and the relative scattering of water and particles, b_w and a_w are the scattering and absorption coefficients for water, b_s and a_s are the sediment specific scattering and absorption coefficients, SPM is the sediment concentration and \tilde{b}_s is the backscatter ratio for sediment. The dominant terms in the remotely sensed reflectance are the scattering, absorption and backscatter ratio of the particles. Models using anomalous diffraction theory (van de Hulst 1957) indicate that the specific scattering coefficients for particles vary from 0.238 to 0.006 m² g⁻¹ ($\lambda = 750$ nm) as particle diameters increase from 5.5 to 100 μ m, whereas the absorption coefficient shows a smaller change, 0.013 to 0.006 m² g⁻¹. Inversion of the IOPs from reported tank experiments shows that the scattering coefficient varies from 0.295 to 0.032 m² g⁻¹ (assuming $\tilde{b}_s = 0.025$ from the San Diego Harbour scattering phase function (Petzold 1972)) and the absorption coefficient varies from 0.022 to 0.011 m² g⁻¹.

Assuming that $\tilde{\rho}$ and ρ are constants dependent on sea state and solar angle, ignoring any spectral variation in Q , n_w and f , and assuming that b_w is insignificant, the band ratio can be modelled by the expression:

$$\frac{\rho_w(\lambda_1)}{\rho_w(\lambda_2)} = \left(\frac{\tilde{b}_s(\lambda_1)}{\tilde{b}_s(\lambda_2)} \right) \left(\frac{b_s(\lambda_1)}{b_s(\lambda_2)} \right) \left(\frac{a_w(\lambda_2) + a_s(\lambda_2) \text{SPM} - r f \tilde{b}_s(\lambda_2) b_s(\lambda_2) \text{SPM}}{a_w(\lambda_1) + a_s(\lambda_1) \text{SPM} - r f \tilde{b}_s(\lambda_1) b_s(\lambda_1) \text{SPM}} \right) \quad (3)$$

As can be seen the ratio is dependent on the spectral backscatter ratio ($\tilde{b}_s(\lambda_1)/\tilde{b}_s(\lambda_2)$), the sediment specific scattering coefficient ($b_s(\lambda_1)/b_s(\lambda_2)$) and the absorption coefficients of water and sediment. Morel and Ahn (1991) demonstrated that the backscatter ratio is spectrally neutral in small organic particles, and observations in turbid waters (Whitlock *et al.* 1981) imply that this is true in waters with suspensions of natural particles. The scattering coefficient will have a λ^{-n} relationship where n depends on the particle size distribution and is typically 1.0 or less, in the range 1.0 to 0.8. The term $b_s(\lambda_1)/b_s(\lambda_2)$ can be replaced by $(\lambda_1/\lambda_2)^{-n}$ or 0.9^{-n} for the 775 nm and 865 nm MERIS bands. Anomalous diffraction theory and tank experiments

show that the absorption coefficient varies only weakly with wavelength, e.g. at a modal diameter of $10\mu\text{m}$ the absorption coefficients are 0.011 , $0.012 \pm 0.001 \text{ m}^2 \text{ g}^{-1}$ at 775 nm and 0.011 , $0.010 \pm 0.001 \text{ m}^2 \text{ g}^{-1}$ at 865 nm , for theory and tank experiments respectively. The reflectance ratio can be further simplified by assuming that, in the NIR, a_s is a constant and wavelength independent for any particle and has only a weak dependence on particle size. The term $a_s(\lambda)\text{SPM} - rf\tilde{b}_b(\lambda)b_s(\lambda)\text{SPM}$ can be summed into a single term $k_s(\lambda)\text{SPM}$, where $k_s = (a_s - rf\tilde{b}_b b_s)$. The sediment absorption term will tend to dominate, since rf is typically around 0.1 . This simplification gives the following expression, which provides an adequate parameterization for the data from tank experiments (figure 2(c)):

$$\frac{\rho_w(\lambda_1)}{\rho_w(\lambda_2)} = \left(\frac{\lambda_1}{\lambda_2}\right)^{-n} \frac{a_w(\lambda_2) + k_s(\lambda_2)\text{SPM}}{a_w(\lambda_1) + k_s(\lambda_1)\text{SPM}} \quad (4)$$

The low contribution from the scattering term explains why these ratios are robust and depend on $a_w(\lambda)$ and SPM concentration only. These ratio methods can be used to determine an approximation for SPM concentration in non-atmospherically corrected data from aircraft sensors (such as CASI) where the sediment load is high and the reflectance from the water is very much larger than the atmospheric path radiance, i.e. conditions where $\rho_{as}(\text{NIR}_1) \ll t\rho_w(\text{NIR}_1)$.

In the visible spectral region, the backscatter from water becomes significant, the absorption from water is less significant and both gelbstoff and chlorophyll absorb in this spectral region. Aiken *et al.* (1995) described the theoretical basis of the band ratio methods for algorithms that relate spectral radiances or reflectances of water to the biogeochemical constituents, using an analytical model parameterized by the IOPs (absorption a and backscatter b_b coefficients of water and the constituents). The reflectance ratios can be approximated by the following expression that has been modified to include the effects of all the constituents of Case II waters:

$$\frac{\rho_w(\lambda_i)}{\rho_w(\lambda_j)} = \frac{b_{bw(i)} + P b_{bp(i)} a_w(j) + G a_{g(j)} + Chl a_{chl(j)} + \text{SPM } a_{s(j)}}{P b_{bp(j)} a_w(i) + G a_{g(i)} + Chl a_{chl(i)} + \text{SPM } a_{s(i)}} \quad (5)$$

If the bands used correspond to wavelengths where there is strong absorption from the dominant constituent, then the double hyperbolic formula applies:

$$\frac{\rho_w(\lambda_1)}{\rho_w(\lambda_2)} = C \frac{1 + X A_1}{1 + X A_2} \quad (6)$$

The inverse is:

$$X = \left[C - \left(\frac{\rho_w(\lambda_a)}{\rho_w(\lambda_2)} \right) \right] / \left[A_2 \left(\frac{\rho_w(\lambda_a)}{\rho_w(\lambda_2)} \right) - C A_1 \right] \quad (7)$$

Where X is the constituent for which the hyperbolic function has been optimized. The constant C is defined as:

$$C = \left(\frac{b_{bw(i)}}{b_{bw(j)}} \right) \left(\frac{a_w(j)}{a_w(i)} \right) \quad (8)$$

Recent work (Moore *et al.* 1997) using Pope and Fry's (1997) figures for the absorption of pure water demonstrate that no empirical tuning of this constant is required.

This basic theoretical form of the band ratio relationships can be used as the

model for algorithms for the other optically active constituents of the water column such as carotenoids, gelbstoff (CDOM) and SPM concentration, and for algorithms using additional (two or more) two-band ratios which compensate for co-existing optically active constituents that may be in significant concentrations. It is used as the theoretical model to derive the 'flag' for waters that are dominated by gelbstoff absorption.

4. Atmospheric model

The atmospheric correction (AC) of remotely sensed radiance (water colour) emanating from Case II waters is a special case for waters with a significant concentration of suspended particulate material, sufficient to generate measurable water leaving radiance at NIR wavelengths (700–1000 nm) termed 'bright pixel' (BP) waters. These circumstances invalidate the conventional AC procedures that have been applied to the CZCS and proposed for MODIS and SeaWiFS (e.g. André and Morel 1991, Gordon and Wang 1994). These algorithms assume that the properties of the atmosphere can be determined from either 'dark pixels' (DP) or by iteration of the single oceanic parameter, chlorophyll. In particular, Gordon and Wang assume that the water-leaving radiance is zero in the NIR SeaWiFS bands (765 and 865 nm) for the DP atmospheric correction scheme.

The problem of atmospheric correction is considered using Gordon and Wang's (1994) SeaWiFS single scattering algorithm. The errors that occur using multiple scattering algorithms (e.g. Antoine and Morel 1998) will be similar, however the effects of significant water-leaving radiance in the NIR are more difficult to define analytically for the multiple scattering case.

The total reflectance at the top of the atmosphere can be written as:

$$\rho_t(\lambda) = \rho_r(\lambda) + \rho_a(\lambda) + \rho_{ra}(\lambda) + \rho_g(\lambda) + t\rho_w(\lambda) \quad (9)$$

where $\rho_t(\lambda)$ is the reflectance at the top of the atmosphere, $\rho_r(\lambda)$ is the reflectance from Rayleigh scattering, $\rho_a(\lambda)$ is the reflectance from aerosol scattering, $\rho_{ra}(\lambda)$ is the reflectance resulting from the interaction of $\rho_r(\lambda)$ and $\rho_a(\lambda)$, $\rho_g(\lambda)$ is the reflectance from the solar beam, t is the diffuse atmospheric transmission and $\rho_w(\lambda)$ is the reflectance of the water. If data are screened for Sun glint, the term $\rho_g(\lambda)$ can be ignored. In the CZCS approximation, the term $\rho_{ra}(\lambda) + \rho_a(\lambda)$ can be approximated by the single scattering approximation $\rho_{as}(\lambda)$. Equation (9) thus becomes:

$$\rho_t(\lambda) = \rho_r(\lambda) + \rho_{as}(\lambda) + t\rho_w(\lambda) \quad (10)$$

In Case I waters in the NIR, the term $t\rho_w(\lambda_{\text{NIR}})$ becomes zero. The term $\rho_r(\lambda_{\text{NIR}})$ can be calculated and thus the term $\rho_{as}(\lambda_{\text{NIR}})$ determined. Given two bands in the NIR it is possible to extrapolate the quantity $\rho_{as}(\lambda)$ using either the conventional Ångström exponent, or using a variable c given in Gordon and Wang (1994). Gordon and Wang (1994) indicate that this extrapolation provides a superior fit for the SeaWiFS bands.

In both these cases

$$\varepsilon_{as}[\lambda_{\text{NIR}}(1), \lambda_{\text{NIR}}(2)] = \rho_{as}[\lambda_{\text{NIR}}(1)] / \rho_{as}[\lambda_{\text{NIR}}(2)] \quad (11)$$

is used to calculate either c or the Ångström exponent, n , where:

$$n = \ln \{ \varepsilon_{as}[\lambda_{\text{NIR}}(1), \lambda_{\text{NIR}}(2)] \} / \ln [\lambda_{\text{NIR}}(1) / \lambda_{\text{NIR}}(2)] \quad (12)$$

and

$$c = \ln \{ \varepsilon_{as}[\lambda_{\text{NIR}}(1), \lambda_{\text{NIR}}(2)] \} / [\lambda_{\text{NIR}}(1) / \lambda_{\text{NIR}}(2)] \quad (13)$$

In the case of the Ångström exponent $\rho_w(\lambda)$ at any wavelength is calculated as:

$$\rho_w(\lambda) = \{\rho_t(\lambda) - \rho_r(\lambda) - \rho_{as}[\lambda_{NIR}(2)] [\lambda/\lambda_{NIR}(2)]^n\}/t \quad (14)$$

and in the case of c , $\rho_w(\lambda)$ is calculated as:

$$\rho_w(\lambda) = \{\rho_t(\lambda) - \rho_r(\lambda) - \rho_{as}[\lambda_{NIR}(2)] \exp[c(\lambda/\lambda_{NIR}(2))]\}/t \quad (15)$$

The transmission term t can be approximated as:

$$t = \exp[-(\tau_r 0.5 + \tau_{oz})/\cos\theta_v] \quad (16)$$

where τ_r is the Rayleigh optical thickness, τ_{oz} is the ozone optical thickness and $\cos\theta_v$ is an approximation to the path length.

In Case II waters $\rho_w(\lambda_{NIR})$ is no longer zero and the observed $\varepsilon[\lambda_{NIR}(1), \lambda_{NIR}(2)]$ becomes:

$$\varepsilon[\lambda_{NIR}(1), \lambda_{NIR}(2)] = \{\rho_{as}[\lambda_{NIR}(1)] + t\rho_w[\lambda_{NIR}(1)]\}/\{\rho_{as}[\lambda_{NIR}(2)] + t\rho_w[\lambda_{NIR}(2)]\} \quad (17)$$

This can be expressed as

$$\begin{aligned} \varepsilon[\lambda_{NIR}(1), \lambda_{NIR}(2)] &= \varepsilon_{as}[\lambda_{NIR}(1), \lambda_{NIR}(2)] + t\{\rho_w[\lambda_{NIR}(1)] \\ &\quad - \varepsilon[\lambda_{NIR}(1), \lambda_{NIR}(2)] \rho_w[\lambda_{NIR}(1)]\}/\rho_{as}[\lambda_{NIR}(2)] \end{aligned} \quad (18)$$

Equation (4) shows that the ratio $\rho_w[\lambda_{NIR}(1)]/\rho_w[\lambda_{NIR}(2)]$ will always be greater than unity, given $a_w(\lambda_{NIR}(1)) > a_w(\lambda_{NIR}(2))$. If the MERIS NIR bands are used then the value of $\rho_w[\lambda_{NIR}(1)]/\rho_w[\lambda_{NIR}(2)]$ will be approximately two, and $\varepsilon[\lambda_{NIR}(1), \lambda_{NIR}(2)]$ will be close to one. Equation (18) may thus be approximated as:

$$\varepsilon[\lambda_{NIR}(1), \lambda_{NIR}(2)] = \varepsilon_{as}[\lambda_{NIR}(1), \lambda_{NIR}(2)] + 0.5t\{\rho_w[\lambda_{NIR}(1)]\}/\rho_{as}[\lambda_{NIR}(2)] \quad (19)$$

Equation (19) shows that any water-leaving radiance in the NIR will result in the observed $\varepsilon[\lambda_{NIR}(1), \lambda_{NIR}(2)]$ being greater than the true $\varepsilon_{as}[\lambda_{NIR}(1), \lambda_{NIR}(2)]$. This will result in overestimation of the Ångström exponent or the parameter c in BP waters. The overestimation of either of these parameters will result in overestimation of the extrapolated $\rho_{as}(\lambda)$ and underestimates or negative values of the resultant $\rho_w(\lambda)$, with the error being worse at lower wavelengths. In areas of moderately high sediment where the atmospheric correction does not actually fail (negative values $\rho_w(\lambda)$), the blue/green ratio will be increased and this will result in anomalously high retrievals of biogeochemical parameters.

In multiple scattering algorithms (e.g. Gordon and Wang 1994, Antoine and Morel 1998) an erroneous estimation of $\varepsilon[\lambda_{NIR}(1), \lambda_{NIR}(2)]$ will result in the choice of the incorrect atmosphere model, with similar but less predictable results.

In order to solve this problem in Case II turbid waters (bright pixel), it is necessary to develop a coupled hydrological and atmospheric optical model in the NIR (700–900 nm) that provides estimates of ρ_{as} that can be used in either a single scattering model or in the multiple scattering models.

5. Implementation

5.1. Introduction

The ‘seamless’ implementation of atmospheric correction and remotely sensed data interpretation is achieved by invoking ‘flags’ for the occurrence of Case II turbid water (denoted II.S) and Case II gelbstoff (denoted II.y) within the processing routines. Figure 1 shows the flow chart for the atmospheric correction scheme, the

Case II turbid water flag and the BP model. It is assumed that for MERIS the Case II.S correction is part of a processing chain using an Antoine and Morel (1998) or Gordon and Wang (1994) type algorithm for determining atmospheric path radiance in Case I waters. However, the method will also work successfully with the single scattering correction (CZCS type correction) outlined above. Initially, data will have been screened for Sun glint, land, ice and clouds. The first stage of the algorithm determines the Rayleigh corrected reflectance:

$$\rho_{rc}(\lambda) = \rho_w(\lambda) + \rho_{as}(\lambda) = \rho_t(\lambda) - \rho_r(\lambda) \quad (20)$$

The second stage of the algorithm determines whether the pixel is contaminated by significant water reflectance in the NIR (Case II.S flag). If the pixel is contaminated, then iterative determinations of the values of $\rho_w(\lambda)$ and $\rho_{as}(\lambda)$ are made.

The third stage of the algorithm uses the $\rho_{as}(\lambda)$ values determined to calculate the aerosol type and the atmospheric turbidity. The $\rho_w(\lambda)$ values are kept for further processing to determine water constituents.

5.2. Turbid water flag

The Case II.S flag is derived by calculating an approximation to the single scattering atmospheric correction of $\rho_w(705)$ described in equations (3) and (4) above. $\varepsilon_{as}(775, 865)$ and n are calculated by assuming that $\rho_w(775)$ and $\rho_w(865)$ are zero, where n is the Ångström exponent calculated from $\varepsilon_{as}(775, 865)$. In Case II.S waters the $\rho_w(705)$ determined is only an approximation to the true $\rho_w(705)$ (see equations (9) and (10)). However the results from LOWTRAN/hydrological models shown in figure 3 indicate that in Case II.S waters this approximate $\rho_w(705)$ has a sharp threshold at around 1 g m^{-3} of SPM. This is where the curves for the different aerosol types converge, and shows that the flag is robust over a range of aerosol types from oceanic to continental. This threshold at present is set at 0.001. Waters where the $\rho_w(705)$ approximation is greater than this are flagged as Case II.S and the iterative correction described below (§5.3) is carried out. In the MERIS architecture, this threshold is assumed to have an angular dependence, and values are stored

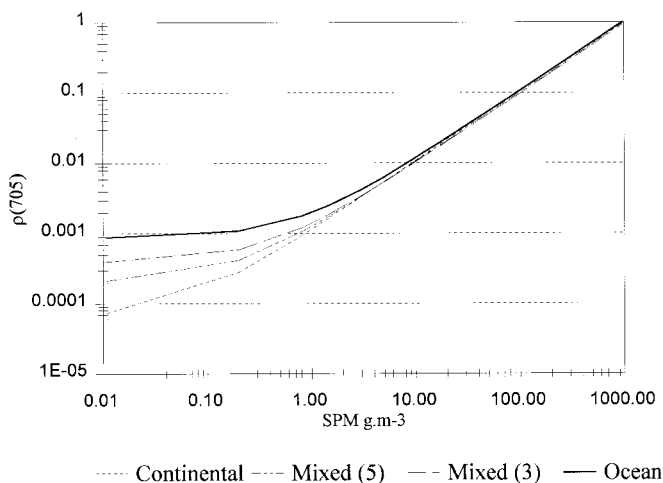


Figure 3. $\rho(705)$ flag compared with sediment concentration. The curves represent the LOWTRAN Navy aerosol types varying from continental to oceanic.

in a look-up table to allow for the angular dependence. Data from pixels that are not flagged are processed by the standard open ocean processing described in §5.4 below.

5.3. Case II correction procedure

In the NIR, it is possible to use a simple single scattering model to estimate $\rho_{as}(NIR)$. The extrapolation parameter used is c of Gordon and Wang (1994) (defined in equation (13)) rather than the conventional Ångström exponent. Give the definition

$$\varepsilon_w(SPM) = \varepsilon_w[\lambda_{NIR}(1) \lambda_{NIR}(2)] = \rho_w[\lambda_{NIR}(1), SPM] / \rho_w[\lambda_{NIR}(2), SPM] \quad (21)$$

the reflectance in the NIR is expressed as

$$\rho_{rc}[\lambda_{NIR}(1)] = t\rho_w[\lambda_{NIR}(2) SPM] \varepsilon_w(SPM) + \rho_{as}[\lambda_{NIR}(2)] \exp\{c[\lambda_{NIR}(1) \lambda_{NIR}(2)]\} \quad (22)$$

where $\rho_w[\lambda_{NIR}(2) SPM]$ is the modelled sediment reflectance. The observed Rayleigh corrected reflectance $\rho_{rc}[\lambda_{NIR}(1)]$ is determined by the three parameters, SPM, $\rho_{as}[\lambda_{NIR}(2)]$ and c . Given measurements at three bands (i.e. two pairs of NIR bands), the parameters $\rho_{as}[\lambda_{NIR}(2)]$, SPM and c can be estimated. The solution method assumes that $\rho_w(\lambda)$ and $\rho_{as}(\lambda)$ have different spectral shapes. In waters where sediment load is extremely high, ε_w will approach ε_{as} and no solution can be found. In practice, this problem has not been found when considering sediment concentrations of up to 100 g m^{-3} . The calculated $\rho_{as}(\lambda_{NIR})$ is input into the Antoine and Morel (1998) open ocean processing chain to determine aerosol type, thickness and path radiance. $\rho_w(\lambda_{NIR})$ may be used to determine near surface sediment load in the Case II.S waters. Within the algorithm the model values of $\rho_w(\lambda, SPM)$ and $\varepsilon_w(SPM)$ are determined by using look-up tables described in Appendix A.

The parameters $\rho_{as}(NIR_1)$, SPM and c are estimated by a four-step procedure (below), using iterative nonlinear equations at steps 2 and 3. The initial guesses at step 1 are calculated using the assumption of an Ångström exponent of unity and assuming that ε_w is fixed for a SPM value of 50 g m^{-3} . Step 2 solves equation (22) with an Ångström exponent of zero. This is a numeric requirement, since both the ρ_{as} and SPM can vary by more than two orders of magnitude, whereas c (or the Ångström exponent) change by only 50%. Step 3 determines c and ρ_{as} with ρ_w fixed.

Step 1. Calculate initial guesses of $\rho_w(865)$ and $\rho_{as}(865)$ (assuming that $\varepsilon_{as} = 1$).

Calculate slope (k) at 50 g m^{-3} SPM:

$$k(775,865) = \rho_w(775, SPM = 50) / \rho_w(865, SPM = 50) \times t - 1.0$$

Solve for $\rho_w(865)$ at this SPM value

$$t\rho_w(865) = \rho_{rc}(865) [\varepsilon(775,865) - 1.0] / k(775,865)$$

$$\text{or } t\rho_w(865) = [\rho_{rc}(775) - \rho_{rc}(865)] / k(775,865)$$

Solve other ρ 's by elimination:

$$\rho_a(865) = \rho_{rc}(865) - t\rho_w(865)$$

$$t\rho_w(775) = \rho_{rc}(775) - \rho_{as}(865)$$

Determine sediment load from $\rho_w(865) / \rho_w(775)$, using a look-up table of the ratio $\varepsilon_w(SPM)$ versus SPM calculated.

Step 2. Determine exact estimates SPM and ρ_{as} by solving the following nonlinear equations, using the Newton–Raphson method.

$$\begin{aligned} 0 &= \rho_{rc}(865) - \rho_w(865, \text{SPM})[t - \rho_{as}(865)] \\ 0 &= \rho_{rc}(775) - \rho_w(775, \text{SPM})[t - \rho_{as}(865)] \end{aligned}$$

This step assumes that the true value of the atmospheric $\varepsilon(775, 865) = 1$.

Step 3. Use the $\rho_{as}(865)$ retrieved in step 2 as an initial estimate to solve a nonlinear equation with variables $\rho_{as}(865)$ and c . Determine Gordon and Wang's c by solving the following equations

$$\begin{aligned} 0 &= \rho_{rc}(865) - \rho_w(865, \text{SPM})[t - \rho_{as}(865)] \\ 0 &= \rho_{rc}(705) - \rho_w(705, \text{SPM})\{t - \rho_{as}(865) \exp[c(705 - 865)]\} \end{aligned}$$

Step 4. Estimate $\rho_{as}(775) = \rho_{as}(865) \times \exp[c(775 - 865)]$

Return $\rho_{as}(775)$, $\rho_{as}(865)$ for further processing by the multiple scattering model.

After the NIR data are corrected for the water reflectance component, the standard Gordon and Wang (1994) aerosol correction procedure is applied. Values for the SPM concentration and the sediment backscatter, b_{bs} , for a shallow surface layer (where NIR optical depth is less than 1 m) are returned from the BP correction scheme.

These estimates will not necessarily be those determined by visible band algorithms since the NIR has lower radiometric sensitivity and the penetration depth at visible wavelengths will be higher. However, at high sediment concentrations, where the turbidities in the visible and NIR are similar, the visible and NIR estimates should converge.

5.4. Atmospheric correction

In the final MERIS processing chain the algorithm of Antoine and Morel (1998) will be used for the determination of atmospheric path radiance. In the current study, a test was carried out using the single scattering algorithm described in §4.

5.5. Gelbstoff dominated water flag

Figure 1 shows the processing chain for the in-water constituents including the Case II.y flag for gelbstoff dominated waters. Gelbstoff (yellow substance) or CDOM of terrestrial or biogenic origin absorbs UV and blue light strongly, with an exponential decrease in absorption towards longer wavelengths. When high concentrations of gelbstoff are present, simple two-band retrieval algorithms using the blue bands give anomalously high chlorophyll (pigment) values because the absorption of co-existing gelbstoff cannot be distinguished from chlorophyll. The magnitude of this anomalous overestimate diminishes for two-band ratio algorithms using the 490: 560 and 510: 560 ratios. In waters with low gelbstoff, estimates of pigment that are based on the absorption at these three wavelengths will be broadly similar. A test which flags the discrepancy of chlorophyll estimation by crude two-band algorithms will indicate high gelbstoff concentrations.

Using the hyperbolic fit described by Aiken *et al.* (1995), three estimates of

pigment are generated: $Chl(442.5, 560)$, $Chl(490, 560)$, $Chl(510, 560)$, where each estimate is based on a reflectance ratio fit:

$$Chl(\lambda_1, \lambda_2) = \left[\left[\frac{\rho_w(\lambda_1)}{\rho_w(\lambda_2)} \right] - A_1 \right] / \left[A_2 - A_3 \times \left[\frac{\rho_w(\lambda_1)}{\rho_w(\lambda_2)} \right] \right] \quad (23)$$

where A_i are constants from empirical fits to *in situ* data. Where $\rho_w(\lambda)$ is zero, the estimate is set at the asymptotic limit of the retrieval. The test does not use the estimate $Chl(412: 560)$ because it is likely that $\rho_w(412)$ will be zero in waters with either high CDOM or pigment concentrations. If the relationship:

$$Chl(443, 555) \geq B_1 \times Chl(490, 560) \geq B_2 \times Chl(510, 560) \quad (24)$$

is satisfied, then the pixel is assumed to be gelbstoff contaminated and the Case II.y flag is set. The constants B_1 and B_2 are fixed at 0.83 from limited field observations. However, they may need to be revised in the light of more extensive data.

5.6. Retrieval of suspended particulate matter

To calculate the concentrations of the optically active in-water constituents, each pixel is processed by a separate algorithm according to the flag status: Case I (no flag); Case II.y (gelbstoff flag); Case II.S (sediment flag). For environmental, physical and bio-optical reasons, these three cases are mutually exclusive in the vast majority (99%) of marine waters. In Case I, by definition, SPM concentrations and gelbstoff are non-existent, though phytoplankton particles and biogenic CDOM can be present and can be retrieved with appropriate algorithms. Likewise, by definition, SPM dominates in Case II.S. Such waters occur in shallow areas of tidally mixed, unstratified shelf seas or in estuarine plumes with high fluvial mud concentrations. Case II.y gelbstoff dominated waters occur in shallow enclosed seas with high land drainage, low tidal mixing and low flushing with the open ocean (e.g. Baltic Sea), or in riverine and estuarine discharges with low concentrations of fluvial muds. Estuarine plumes can have significant concentrations of both SPM and gelbstoff co-existing but only one will dominate the water colour and the flagging procedures will select which processing scheme will be applied.

In terms of the MERIS processing architecture, Case I waters will be processed by algorithms described by Bricaud *et al.* (1999) and their processing will not be described further here. The Case II algorithms use two ratio methods, differing in the number of wavelengths available. Case II.S waters show significant reflectance from 440 nm to 800 nm, with the lower wavelength limit depending on the gelbstoff concentration. In contrast, those waters that have been determined as Case II.y have no significant reflectance in the NIR, and will only show significant reflectance in the 443–620 nm region. Waters with extremely high concentrations of gelbstoff may be effectively black and prove intractable to any quantitative algorithm.

In the validation described here, only the ratio SPM algorithm described in §3 has been used. To date, the waters tested have all been flagged as Case II.S. Although the Case II.y flag has been tested with model data, empirical observations of this water type are lacking. The full biogeochemical algorithms and their model testing will be described in a future publication.

6. Field studies

The case study used CASI imagery acquired over the Humber Estuary by the NRA (National Rivers Authority) survey operations on 1 September 1993. The

flightlines were from the south bank of the Humber, north-eastward, east of Spurn Point into 'clear' North Sea water beyond the Humber Plume (see figure 4).

The raw image of flightline 1 is shown in figure 5(a); land, the south bank of the Humber, and a cloud streak are at the bottom of the image. Prior to correction, the true colour composite from CASI bands at 670, 510 and 448 nm, printed as the corresponding red blue and green colours, shows a distinctive blue 'haze', with white wispy patches in places where there are thin clouds or high concentrations of aerosols (see figure 5(a)). The AC using the dark pixel method (shown as a colour composite in figure 5(b)) has removed the blue 'haze' and the white wispy patches, leaving blue water in places and coloured water elsewhere. However, the plume area has been 'over corrected', generally showing only water-leaving radiance in the red as the AC procedure generated negative and near-zero water-leaving radiances in the blue and green. Any land or clouds are masked black in all the AC processes. Figure 5(c) shows the $\epsilon(775, 865)$ map as a grey scale image, derived from the dark pixel AC process. This shows high values of $\epsilon(775, 865)$ in the plume where sediment levels are high; the anomalous $\epsilon(775, 865)$ matches the area where the atmospheric correction has failed. After the bright pixel AC (see figure 5(d)), this qualitative description changes. The true colour composite shows bright blue water in places, green water elsewhere, and bright orange to brown patches where there are high SPM concentrations. Everywhere the AC procedure generated positive water-leaving radiances in the blue and green. These results indicate that the procedures are producing qualitatively correct water-leaving radiances. Incorrect performance of the procedures would produce skewed-colour or 'black' images, when over corrected and negative radiances are calculated. Swath-width banding or limb-brightening would show up where the AC procedures are not operating correctly over the full angular width of the swath.

Figure 6 shows the derived SPM maps (grey scale) for flightlines 1 and 5. Flightline 5 was flown 21 minutes later and over the same flight direction as flightline 1 but at a height of 1500 m. Flightline 1 has clear water adjacent to the coast at the top of the image (SPM concentration $< 4 \text{ g m}^{-3}$, possibly zero) and low reflectance water north of this (SPM concentration $4\text{--}8 \text{ g m}^{-3}$). The plume has a high SPM outer halo and an intense core (SPM concentrations of $12\text{--}16$ and $33\text{--}38 \text{ g m}^{-3}$ respectively). The survey vessel is in an area of quite low SPM concentration (around 9 g m^{-3}). To the north-east, in the clear North Sea waters, the SPM values are not measurable. Flightline 5 shows the same plume structure as observed in flightline 1. There is noise and along-track banding, probably due to an incorrect set-up of the instrument for the lower flight height.

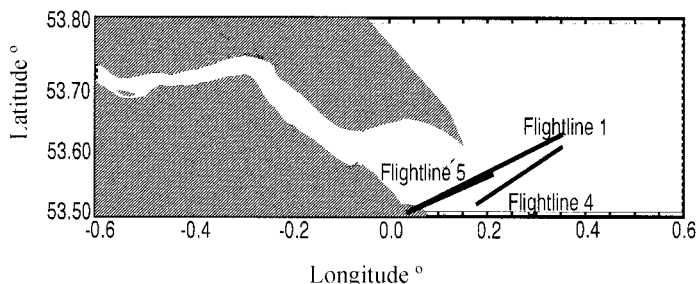


Figure 4. Geographical positions of flightlines 1, 4 and 5, Humber Estuary.

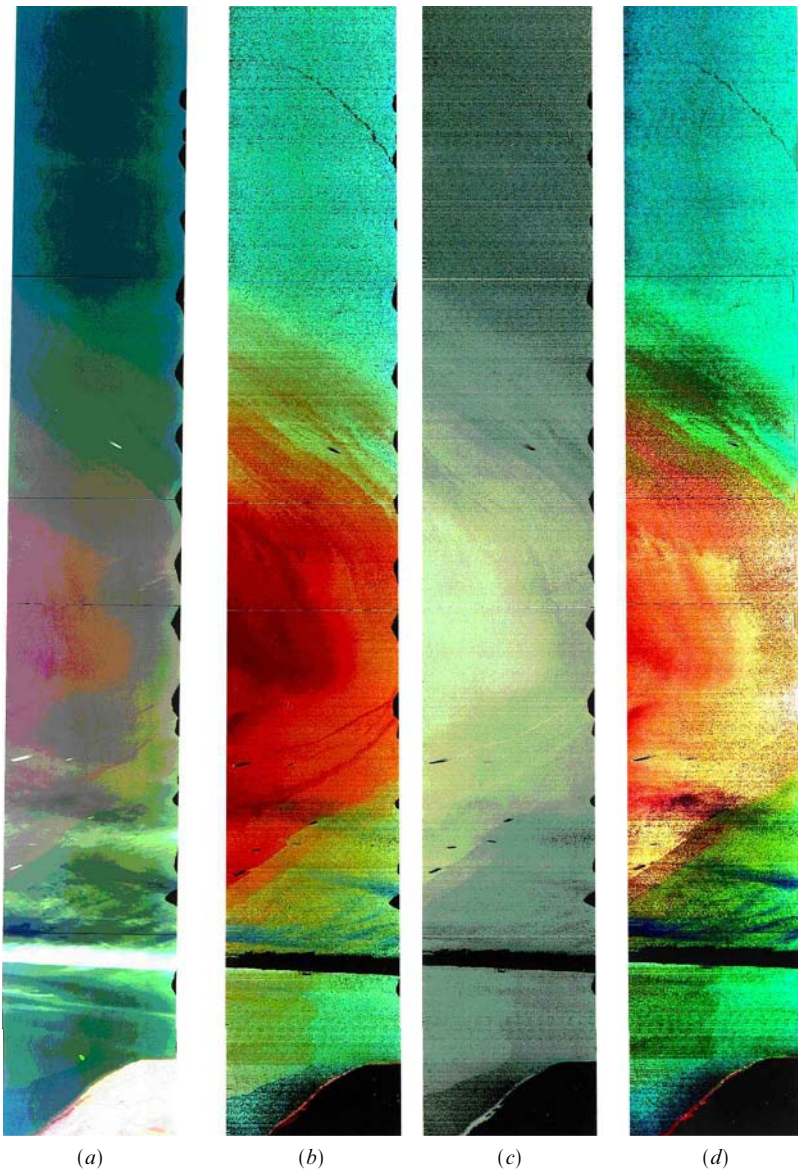


Figure 5. Atmospheric correction stages for flightline 1, at 3000 m, south bank of the Humber Estuary into the North Sea at 11:54 GMT on 1 September 1993. (a) Uncorrected colour composite using bands at 448, 510 and 670 nm. (b) Dark pixel corrected colour composite. (c) $\epsilon(775, 865)$ map. (d) Bright pixel corrected colour composite.

7. Validation

The test case described used a minimal data set but provided an excellent opportunity for validation of the atmospheric correction procedures. The data from the flights were obtained over the same stretch of water, within a short interval and had simultaneous sea-truth measurements carried out on the NRA ship *Sea Vigil*.

Figure 7(a) shows a comparison of the multispectral radiances from two zones within flightline 1: Case I water (northern end of flightline) and Case II water (inner

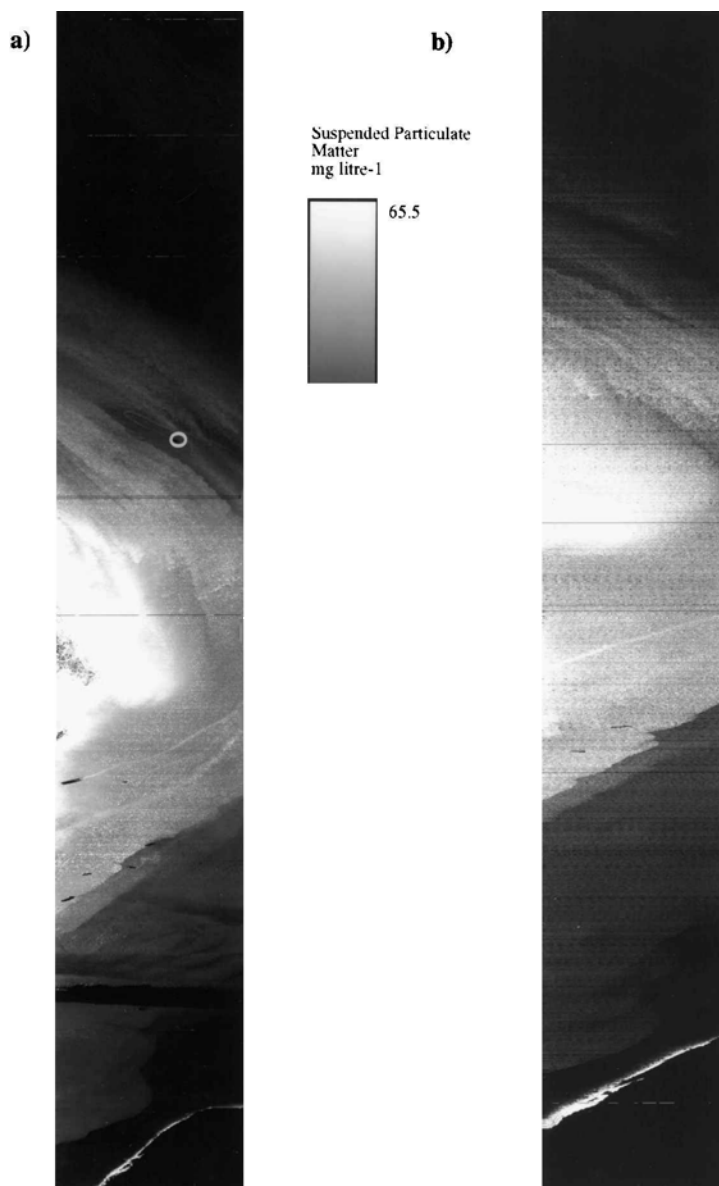


Figure 6. (a) SPM map (g m^{-3}) derived from flightline 1, at 3000m, 11:54 GMT on 1 September 1993. The position of *Sea Vigil* marked. (b) SPM map (g m^{-3}) derived from flightline 5, at 1500m, 12:14 GMT on 1 September 1993.

plume area). The figure shows the uncorrected radiances; the dark pixel corrected and the bright pixel corrected spectra are shown for each zone. Within the plume area, the dark pixel procedure results in over corrected spectra with zero radiances for both the blue and NIR bands. For the Case I water, both procedures produce the same spectra, indicating that the Case II.S flag is performing correctly.

Figure 7(b) shows the uncorrected and atmospherically corrected multi-spectral radiances from the sequential flights at 3000 m (flightline 1), 1500 m (flightline 5,

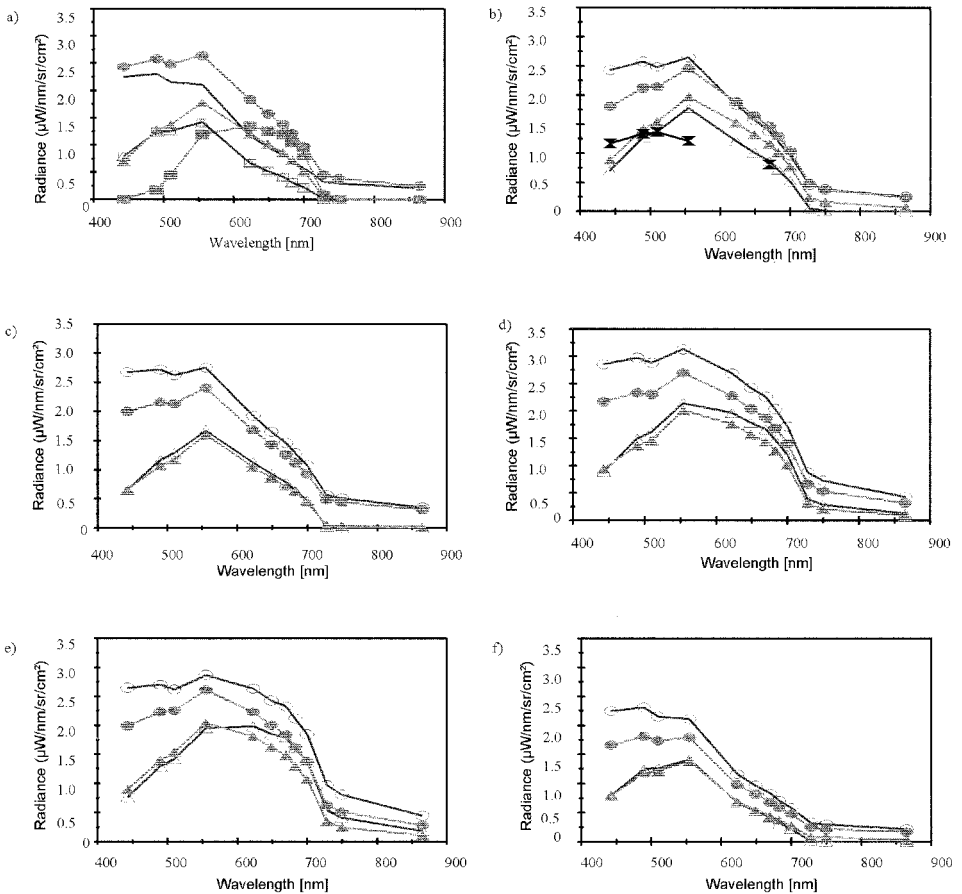


Figure 7. (a) Uncorrected (circles), dark pixel corrected (squares) and bright pixel corrected (triangles) pixels from Case I[B] (unfilled symbols) and Case II[P] (filled symbols) water masses for flightline 1, 1 September 1993. (b) Uncorrected (circles) and corrected (triangles) radiances for flightline 1 (unfilled symbols) [3000 m] and flightline 5 (filled symbols) (1500 m), 1 September 1993 and the measured water-leaving radiance (hour-glasses) using the PRR-600 deployed from the survey vessel. (c)–(f) Uncorrected (circles) and corrected (triangles) radiances for flightline 1 (unfilled symbols) (3000 m) and flightline 5 (filled symbols) (1500 m), 1 September 1993. Zones are: (c) low turbidity water; (d) outer plume; (e) inner plume; (f) Case I water.

20 minutes later) and the water-leaving radiance from an *in situ* profile of the Biospherical Instruments, Profiling Reflectance Radiometer (PRR-600) in the water simultaneous with flightline 5. The two airborne radiances return almost identical values for the water signals, after the full atmospheric correction, and the measured in-water data agree at three wavelengths (490, 510 and 670 nm). The disagreement on the retrieved radiances and the measured radiance at 555 nm would appear to be a radiometric (calibration) problem with the CASI measurements. There are no known spectral features of the atmosphere, water or SPM that would account for this ‘peaked’ feature in the spectra. Indeed the ‘in-water’ spectra from the PRR-600 look smooth from 510 to 555 to 670 nm and correspond to expectations from published data. The divergence of the data in the blue is small and could arise from

measurement problems with either the CASI or the PRR-600, since sensitivity of calibration and accuracy decrease at the blue wavelengths.

Figure 8 shows the SPM, at nadir, for both flightlines 1 and 5 derived from (a) a visible ratio algorithm determined from tank measurements as described earlier, and (b) the NIR algorithm, used in the iterative bright pixel atmospheric correction; along-track the data were binned to represent MERIS pixels (250 m). There is good agreement for the data from the two flightlines, temporally separated by 20 minutes, even for this fast flowing dynamic estuary. Both data from the different algorithms

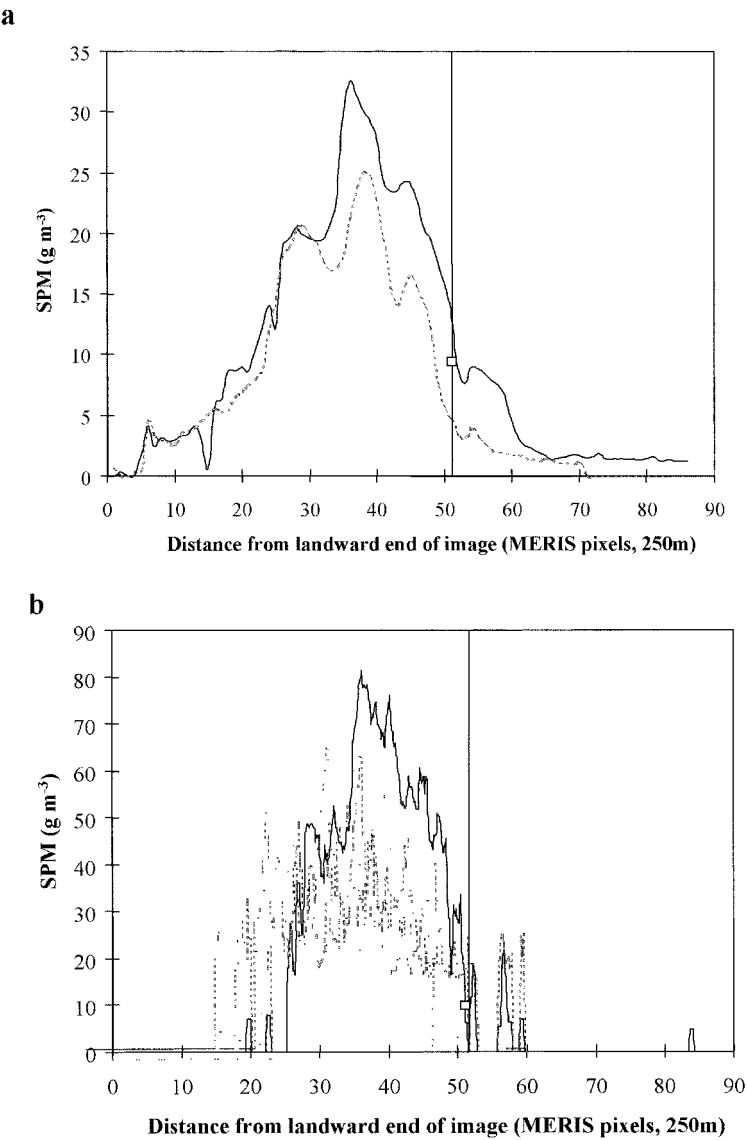


Figure 8. (a) Plot of visible band SPM for September flightline 1 (solid line) and flightline 5 (dotted line). (b) Plot of NIR band SPM for September flightline 1 (solid line) and flightline 5 (dotted line). The vertical lines mark the position of *Sea Vigil*, and the square symbols give the retrieved SPM values from the imagery.

show similar patterns, with a peak around 40 pixels from land, corresponding to the sediment plume shown in the images (figure 5). The NIR derived SPM shows values of zero in areas where there is no significant water-leaving radiance in the NIR. The visible band algorithm retrieves SPM values of 2.5 or less in these areas.

The retrieved SPM values are lower away from land in flightline 5 compared to flightline 1. This may be caused by flightlines having different headings—flightline 5 going to the east of flightline 1, where the plume was less intense. The values of the peak SPM concentration for the two algorithms are a factor of two different. However, the values at the position of the *Sea Vigil* are comparable: flightline 1 = 13.8 and 4.6 gm^{-3} ; flightline 5 = 12.6 and 18.0 gm^{-3} (mean = 12.3 gm^{-3}) for the visible and NIR algorithms respectively. The similarity of the results from these algorithms at lower SPM concentrations may indicate that the visible algorithm is saturating at higher concentrations. Comparisons with the *Sea Vigil* measurement show that the remotely sensed values give higher estimates compared with *in situ* measurements. The *in situ* values measured were 9.4 and 9.9 for flightlines 1 and 5 respectively, compared with 13.8/4.6 and 12.6/18.0 for the visible/NIR remotely sensed algorithms. This difference may be caused either by depth structure or by navigation problems. The *in situ* measurements were taken at more than 2 m depth. The remotely sensed depth for the visible and NIR algorithms was 1 m and 0.25 m respectively. Local disturbance of sediments is shown by the brighter ship tracks of vessels (see figure 6(a)). Navigation errors are also a problem, since the *Sea Vigil* was at the edge of the plume where an error of two MERIS pixels can dramatically change the derived SPM values. The position of *Sea Vigil* is marked in figure 6(a).

With the exception of the remotely sensed NIR measurement for flightline 5, where the data showed noise, all the remote sensed measurements are within 50% of the *in situ* measurements. This is encouraging, since the algorithms are based on experimental observations and theoretical models for a range of UK coastal sediment types, with no specific 'tuning' to match the specific Humber sediments. Further observations, with better navigation, are required to determine if the retrieval methods can achieve a better accuracy than $\pm 50\%$ over a range of sites.

8. Conclusion and discussion

Algorithm testing and validation presents major problems for both Case I and II waters. The validation system was designed for the Case II waters around the LOIS (Land Ocean Interaction Study, UK contribution to LOICZ) study region, remote sensing activities in the Humber estuary (1993 campaign) with the CASI sensor and a contemporary sea truth campaign. It is necessary to compare remote sensor corrected radiances (CASI) with water-leaving radiances determined from *in situ* measurements. Generally, this provides only one point per flight, which is a less than adequate validation in a fast moving estuary such as the Humber. The same limitations and restrictions apply to secondary validation, where measured biogeochemical parameters are compared with derived values (one point per flight). Spatially extensive, though qualitative, validation can be achieved by comparing data (radiances or derived products) from flights at two different heights over the same stretch of water. These data can be made absolute if sea truth data are available to provide validation even at a single point.

Appendix A: derivation of reflectance tables

The atmospheric correction requires the calculation of above water reflectance that corresponds to a suspended particulate concentration. The value of

$\rho_w(\lambda, \text{SPM}, [\theta_s, \theta_v, \Delta\phi])$ is determined by a two stage look-up of a tables of $\rho_w(\lambda, a, b, [\theta_s, \theta_v, \Delta\phi])$ and tables of $a(\text{SPM}), b(\text{SPM})$. At present, the tables of $a(\text{SPM}), b(\text{SPM})$ are a linear look-up of the values given in §2. However the dual look-up table approach allows the rapid incorporation of new sediment IOPs into the algorithm. A common set of IOP versus reflectance look-up tables can also be used across a suite of algorithms for other biogeochemical variables, i.e. gelbstoff and chlorophyll concentrations.

The reflectance tables are generated from Mobley’s Hydrolight Model (Mobley 1995), for the set of view angles given in table A1. The look-up tables are offset by the values of the pure water a and b . The calculations are carried out assuming the San Diego harbour phase function of Petzold (1972). The tables are interpolated using linear interpolation with reciprocal weighting. The table data requirements are 3 M byte per band, and present no storage problems for the atmospheric correction procedure.

Table A1.

Dimension	Values	Range
λ	10	412.5,442.5,490,510,560,620,665,705,775,865
a^a	16	0.0,0.01 100 in log increments
b^a	16	0.0,0.01 40 in log increments
θ_v	8	0°,5° 35°
θ_s	8	0°,10° 70°
$\Delta\phi$	12	0°,30° 330°

^a Actual value in table ($a-a_w$).

References

AIKEN, J., MOORE, G. F., TREES, C. C., HOOKER, S. B., and CLARK, D. K., 1995, The SeaWiFS CZCS-Type Pigment Algorithm. NASA Technical Memorandum 104566, Vol. 29, edited by S. B. Hooker and E. R. Firestone, NASA Goddard Space Flight Center, Greenbelt, Maryland, USA.

ANDRÉ, J.-M., and MOREL, A., 1991, Atmospheric corrections and interpretation of marine radiances in CZCS imagery, revisited. *Oceanologica Acta*, **14**, 3–22.

ANTOINE, D., and MOREL, A., 1998, Relative importance of multiple scattering by air molecules and aerosols in forming the atmospheric path radiance in the visible and near infra-red parts of the spectrum. *Applied Optics*, **37**, 2245–2259.

BALE, A. J., TOCHER, M. D., WEAVER, R., HUDSON, S. J., and AIKEN, J., 1994, Laboratory measurements of the spectral properties of estuarine suspended particles. *Netherlands Journal of Aquatic Ecology*, **28**, 237–244.

BRICAUD, A., MOREL, A., and BARALE, V., 1999, MERIS potential for ocean colour studies in the open ocean. *International Journal of Remote Sensing*, **20**, 1757–1769 (this issue).

BRICAUD, A., MOREL, A., and PRIEUR, L., 1981, Absorption by dissolved organic matter to the sea (yellow substance) in the UV and visible domains. *Limnology and Oceanography*, **26**, 45–53.

DUYSENS, L. N. M., 1956, The flattening of the absorption spectrum of suspensions as compared with that of solutions. *Biochimica et Biophysica Acta*, **19**, 255, 257, 261.

GORDON, H. R., and DING, K., 1992, Shelf shading of in-water optical instruments. *Limnology and Oceanography*, **37**, 491–500.

GORDON, H. R., and WANG, M., 1994, Retrieval of water-leaving radiance and aerosol optical thickness over the oceans with SeaWiFS: a preliminary algorithm. *Applied Optics*, **33**, 443–452.

MOBLEY, C. D., 1995, *Hydrolight 3.0 Users Guide*, SRI Project 5632.

- MOBLEY, C. D., GENTILI, B., GORDON, H. R., JIN, G., KATTAWAR, A., MOREL, A., RENERSMAN, P., STAMMES, K., and STAVN, R. H., 1993, Comparison of numerical models for computing underwater light fields. *Applied Optics*, **32**, 7484–7504.
- MOREL, A., 1974, Optical properties of pure water and sea water. *Optical Aspects of Oceanography*, edited by N. G. Jerlov and S. Nielsen (New York: Academic), pp. 1–24.
- MOREL, A., and AHN, Y. H., 1991, Optics of heterotrophic nanoflagellates and ciliates. A tentative assessment of their scattering role in oceanic waters compared to those of bacterial and algal cells. *Journal of Marine Research*, **49**, 177–202.
- MOREL, A., and GENTILI, B., 1991, Diffuse reflectance of oceanic waters. I. Its dependence on sun angle as influenced by the molecular scattering contribution. *Applied Optics*, **30**, 427–4, 438.
- MOREL, A., and GENTILI, B., 1993, Diffuse reflectance of oceanic waters. II. Bi-directional aspects. *Applied Optics*, **32**, 864–6, 879.
- MOORE, G., AIKEN, J., HOOKER, S. B., and REES, N., 1997, Remote sensing of bio-optical provinces. *RSS 1997, Observations and Interactions*, pp. 545–550.
- PALMER, K. F., and WILLIAMS, D., 1974, Optical properties of water in the near infra-red. *Journal of the Optical Society of America*, **64**, 1107–1110.
- POPE, M. R., and FRY, E. S., 1997, Absorption Spectrum (380–700 nm) of pure water. II. Integrating cavity measurements. *Applied Optics*, **36**, 8710–8723.
- RAST, M., and BEZY, J-L., 1999, The MERIS instrument. *International Journal of Remote Sensing*, **20**, 1681–1702 (this issue).
- PETZOLD, T. J., 1972, Volume scattering functions for selected ocean waters. *Scripps Institute of Oceanography Report*, **72–78**, 79.
- VAN DE HULST, H. C., 1957, *Light Scattering by Small Particles* (Chichester: Wiley).
- VOLGIN, V. M., YERSHOV, O. A., SMIRNOV, A. V., and SHIFRIN, K. S., 1988, Optical depth of aerosol in typical sea areas. *Izvestiya, Atmospheric & Oceanic Physics*, **24**, 772–777.
- WHITLOCK, C. H., POOLE, L. R., USRY, J. W., HOUGHTON, W. M., WITTE, W. G., MORRIS, W. D., and GURGANUS, E. A., 1981, Comparison of reflectance with backscatter and absorption parameters for turbid waters. *Applied Optics*, **20**, 517–522.